WALLABY Pilot Survey: Hydra Cluster Galaxies UV and HI morphometrics

Benne W. Holwerda, Frank Bigiel, Albert Bosma, Helene M. Courtois, Nathan Deg, Helga Dénes, Ahmed Elagali, Bi-Qing For, Baerbel Koribalski, Denis A. Leahy, et al.

Monthly Notices of the ROYAL ASTRONOMICAL SOCIETY

MNRAS **521,** 1502–1517 (2023) https://doi.org/10.1093/mnras/stad602
Advance Access publication 2023 February 28

WALLABY Pilot Survey: hydra cluster galaxies UV and H I morphometrics

Benne W. Holwerda [1★] Frank Bigiel,[2] Albert Bosma [3] Helene M. Courtois,[4] Nathan Deg,[5] Helga Dénes,[6] Ahmed Elagali,[7] Bi-Qing For [7,8] Baerbel Koribalski [8,9,10] Denis A. Leahy [11] Karen Lee-Waddell [7,12] Ángel R. López-Sánchez,[8,13,14,15] Se-Heon Oh,[16] Tristan N. Reynolds [7,8] Jonghwan Rhee,[7,8] Kristine Spekkens,[17] Jing Wang,[18] Tobias Westmeier [7,8] and O. Ivy Wong [7,8,12]

[1]*University of Louisville, Department of Physics and Astronomy, 102 Natural Science Building, Louisville, KY 40292 USA*
[2]*Argelander-Institut für Astronomie, Universität Bonn, Auf dem Hügel 71, D-53121 Bonn, Germany*
[3]*Aix Marseille University, CNRS, CNES, LAM, F-13013 Marseille, France*
[4]*Univ Lyon, Univ Claude Bernard Lyon 1, IUF, IP2I Lyon, F-69622, Villeurbanne, France*
[5]*Department of Physics, Engineering Physics, and Astronomy, Queen's University, Kingston, ON, K7L 3N6, Canada*
[6]*ASTRON, Netherlands Institute for Radio Astronomy, 7991 PD Dwingeloo, the Netherlands*
[7]*ICRAR, The University of Western Australia, 35 Stirling Highway, Crawley WA 6009, Australia*
[8]*ARC Centre of Excellence for Astrophysics in 3 Dimensions (ASTRO 3D), Stromlo, ACT 2611, Australia*
[9]*Australia Telescope National Facility, CSIRO Space & Astronomy, PO Box 76, Epping, NSW 1710, Australia*
[10]*School of Science, Western Sydney University, Locked Bag 1797, Penrith, NSW 2751, Australia*
[11]*Department of Physics and Astronomy, University of Calgary, 2500 University Dr. NW, Calgary T2N 1N4, Canada*
[12]*Australia Telescope National Facility, CSIRO Space & Astronomy, PO Box 1130, Bentley, WA 6102, Australia*
[13]*Australian Astronomical Optics, Macquarie University, 105 Delhi Rd, North Ryde, NSW 2113, Australia*
[14]*Department of Physics and Astronomy, Macquarie University, NSW 2109, Australia*
[15]*Macquarie University Research Centre for Astronomy, Astrophysics & Astrophotonics, Sydney, NSW 2109, Australia*
[16]*Department of Physics and Astronomy, Sejong University, 209 Neungdong-ro, Gwangjin-gu, Seoul, Republic of Korea*
[17]*Department of Physics and Space Science, Royal Military College of Canada, PO Box 17000, Station Forces, Kingston, Ontario, K7K 7B4, Canada*
[18]*Kavli Institute for Astronomy and Astrophysics, Peking University, Beijing 100871, China*

Accepted 2023 February 14. Received 2023 February 14; in original form 2022 June 6

ABSTRACT

Galaxy morphology in atomic hydrogen (H I) and in the ultraviolet (UV) are closely linked. This has motivated their combined use to quantify morphology over the full H I disc for both H I and UV imaging. We apply galaxy morphometrics: concentration, asymmetry, gini, M_{20} and multimode-intensity-deviation statistics to the first moment-0 maps of the WALLABY Survey of galaxies in the hydra cluster centre. Taking advantage of this new H I survey, we apply the same morphometrics over the full H I extent on archival GALEX *FUV* and *NUV* data to explore how well H I truncated, extended ultraviolet disc (XUV) and other morphological phenomena can be captured using pipeline WALLABY data products. Extended H I and UV discs can be identified relatively straightforward from their respective concentration. Combined with WALLABY H I, even the shallowest GALEX data are sufficient to identify XUV discs. Our second goal is to isolate galaxies undergoing ram-pressure stripping in the H I morphometric space. We employ four different machine learning techniques, a decision tree, a k-nearest neighbour, a support-vector machine, and a random forest. Up to 80 per cent precision and recall are possible with the random forest giving the most robust results.

Key words: galaxies: disc – galaxies: ISM – galaxies: kinematics and dynamics – galaxies: spiral – galaxies: statistics – galaxies: structure.

1 INTRODUCTION

In principle, the appearance of galaxies is a direct result of the processes that formed and shaped them. Turning their appearance into a qualified value, while accounting for viewing angle is a long-standing undertaking in observational extragalactic astronomy.

While most morphology quantifications focus on the stellar component of galaxies, a very information-rich view of gas-rich galaxies is the 21-cm line emission of neutral hydrogen (H I). This gas spans most often a larger disc than the stars, and it is considered more sensitive to early interaction (e.g. Hibbard et al. 2001). There is an active interest in the outskirts of spiral galaxy discs because they are the sites of the most recent, readily observable acquisition of gas for these systems (e.g. Sancisi et al. 2008) and low-level star formation (e.g. Dong et al. 2008; Koribalski & López-Sánchez 2009; Bigiel et al. 2010; Alberts et al. 2011; López-Sánchez et al. 2015; Watson et al. 2016).

This low-level star formation was first discovered in Hα emission by Ferguson et al. (1998) and Lelièvre & Roy (2000) and later

★ E-mail: benne.holwerda@gmail.com

in *GALEX* ultraviolet (UV) imaging as extended ultraviolet (XUV) discs (Thilker et al. 2005a, b, 2007; Gil de Paz et al. 2005, 2007; Zaritsky & Christlein 2007; Lemonias et al. 2011; Koribalski 2017; Meurer 2017). These XUV disc complexes are generally ∼100 Myr old, which explains why most lack Hα (Alberts et al. 2011). UV knots in interactions may be an exception (López-Sánchez et al. 2015). A different explanation, i.e. a top-light initial mass function (IMF), as proposed by Meurer et al. (2009), Koda et al. (2015), Bruzzese et al. (2015), and Watts et al. (2018), remains a possibility, but the IMF is stochastically sampled. The metallicities of these complexes, as derived from emission lines, are subsolar, in the range of 0.1–1 $Z_{\odot}$ Gil de Paz et al. (2007), Bresolin et al. (2009), Werk et al. (2010), and López-Sánchez et al. (2015).

It was noted early by several authors that the atomic hydrogen as observed by the 21-cm fine structure line and the UV structure seem closely related. That the H I disc that extends well beyond the optical disc of spiral galaxies has been known for a long time (e.g. Bosma 1978; Begeman 1989; Meurer et al. 1996; Meurer, Staveley-Smith & Killeen 1998; Swaters et al. 2002; Noordermeer et al. 2005; Boomsma et al. 2008; de Blok et al. 2008; Walter et al. 2008; Elson, de Blok & Kraan-Korteweg 2011; Heald et al. 2011b, a; Zschaechner et al. 2011) but only recently the close correlation with UV structure drove a direct comparison (cf. de Paz et al. 2008; Lemonias et al. 2011).

A lopsided appearance of the outer H I disc (Jog & Combes 2009; van Eymeren et al. 2011a,b) or an asymmetry (Giese et al. 2016; Reynolds et al. 2020) can have a myriad of internal or external processes responsible for it: accretion along cosmic web filaments (Bournaud, Jog & Combes 2005), minor satellite accretion (Zaritsky & Rix 1997), tidal interactions (Jog & Combes 2009; Koribalski & López-Sánchez 2009), ram-pressure stripping (RPS; Moore & Gottesman 1998; Hess et al. 2022), and sloshing within the dark matter halo (Stinson et al. 2009). The anecdotal similarity and the potential common origin of gas accretion is what drove the use of morphometrics on combined data sets (Holwerda et al. 2011b; Holwerda, Pirzkal & Heiner 2012).

Parametrization of H I disc appearance is different from stellar parametrization because the H I disc is based on line emission and therefore has a lower dynamic range. The area covered by the disc is larger, but the spatial resolution is typically an order of magnitude lower due to the much larger H I beam (or Point Spread Function).

A good companion data set is typically GALEX UV [far-UV (FUV) and near-UV (NUV)] because the spatial sampling is often similar to H I scales, and H I and the UV from newly formed young stars are related in distribution (Thilker et al. 2005a; Gil de Paz et al. 2005) and possibly linked through mutual formation processes (Heiner, Vázquez-Semadeni & Ballesteros-Paredes 2014; López-Sánchez et al. 2018). The main benefit of using both H I and UV imaging information is that UV images are inherently very clumpy in appearance. It becomes increasingly difficult to distinguish which UV source is a star-forming region belonging to the disc and which is a background source. By using the H I outer contour, the extent of the UV disc can be identified more reliably (e.g. the discussion on outermost H II regions in Hunter et al. 2018).

In this paper, we apply the galaxy morphometrics originally developed for stellar discs, which were applied with some success on H I data in the past (Holwerda et al. 2011a,b,c,d,e; Holwerda et al. 2012; Giese et al. 2016; Reynolds et al. 2020) but on often heterogeneous data. For example, Giese et al. (2016) pointed out that these depend strongly on the signal-to-noise ratio (s/n) of each object, complicating their use across surveys or with varying s/n. The optimal application is therefore within a single survey although careful comparisons can successfully be made between instrument setups of different surveys (Reynolds et al. 2020). We use the STATMORPH implementation of these morphometrics (Rodriguez-Gomez et al. 2019).

Starting with the early Widefield ASKAP L-band Legacy All-sky Blind surveY (WALLABY) data (Serra et al. (Serra et al. 2015b; Elagali et al. 2019; For et al. 2019; Kleiner et al. 2019; Lee-Waddell et al. 2019; Reynolds et al. 2019; Koribalski et al. 2020), we apply the image morphometrics on H I and *GALEX* FUV data to explore their utility in identifying disturbed H I discs, H I deficient or truncated discs, and extended UV discs. This paper is organized as follows: Section 2 describes the early WALLABY Australian SKA Pathfinder (ASKAP) and *GALEX* data products used; Section 3 describes the morphometrics employed on both H I and *GALEX* imaging; Section 4 describes the results for morphometrics to identify extended and ram-pressure stripped discs; Section 5 describes the H I morphometrics of ram-pressure galaxies; Section 6 describes the machine learning (ML) applied to the H I morphometric space to identify RPS galaxies; and Section 7 briefly discusses all of our results and a future outline of their potential use in WALLABY survey proper. Throughout, we use the Planck (2015) cosmology ($H_0 = 67.74$ km/s/Mpc, $\Omega_0 = 0.3075$, Planck Collaboration 2016).

2 WALLABY SURVEY

The WALLABY (Koribalski et al. 2020) is one of several key surveys that will soon begin on the ASKAP (Johnston et al. 2008, 2007; Johnston 2007; Johnston, Feain & Gupta 2009; Hotan et al. 2014, 2021; McConnell et al. 2016; Koribalski 2022), which is an imaging radio telescope located at the Murchison Radio-astronomy Observatory in Western Australia. The aim of WALLABY is to use the powerful wide-field phased-array technology of ASKAP to observe a large fraction of the whole sky in the 21-cm line of H I at 30-arcsec angular resolution, which will yield information for hundreds of thousands of external galaxies in the local Universe.

Science goals include an understanding of the role of stellar and black hole feedback, gas accretion, and galaxy interactions in galaxy evolution. Currently, the WALLABY Pilot Survey observations covered three 60 deg^2 fields, of which the hydra field is one. The Pilot survey is allowing the team to develop, deploy, and commission its pipeline processing, data verification, and post-processing algorithms, as well as measure the properties of hundreds of galaxies, including their distance, neutral hydrogen mass, and total mass.

2.1 Hydra cluster field

The hydra field was observed with ASKAP as part of the WALLABY Pilot Survey. The first and second internal data releases (hydra TR1 and TR2) are available in the sense that the original data cubes produced by the ASKAP pipeline are available to team members on the CSIRO data archive CSIRO ASKAP Science Data Archive (CASDA). In addition, WALLABY has run its own SOFIA software (Serra et al. 2015a; Westmeier et al. 2021) to produce source catalogues and source images/spectra for the team to work on. The WALLABY team internal data release covers a subregion of the core of the hydra cluster in a region of the cube that is relatively clean from artefacts (Reynolds et al. 2021; Wang et al. 2021). The region covers the RA range of approximately 10:32:00 to 10:45:00 and the declination range of approximately −30:20:00 to −24:40:00, corresponding to about 5.5 × 3.5 degrees on the sky or roughly one-third of the eventual full hydra field (Fig. 1). The redshift range

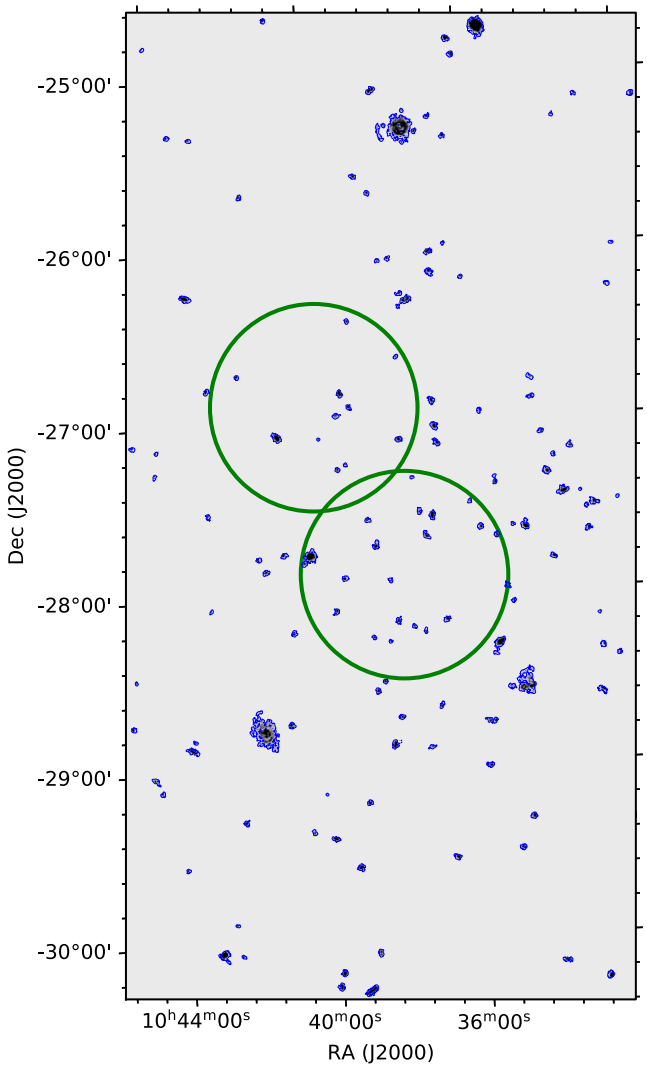

Figure 1. The moment-0 map of the central part of the hydra cluster with H I detections outlined in blue (set to 10 Jy/beam×Hz in the moment-0). The location of the two *GALEX* fields are outlined in green. The full TR2 coverage extends to either side.

considered here covers cz $= 500$–$15000\ \mathrm{km\,s^{-1}}$ ($z < 0.05$), roughly half of the Radio Frequency Interference (RFI)-free band available to WALLABY.

In order to reduce the impact of residual continuum emission on the source finding, the positions of all NRAO VLA Sky Survey (NVSS; Condon et al. 1998) sources with a flux density in excess of 150 mJy were manually flagged in the form of a box of size 11 × 11 pixels centred on the pixel containing each NVSS position.

The great benefit for calculating morphometrics in this field is that the galaxies are all at comparable distances and the observations all probe similar spatial scales.

2.2 SOFIA source finding

H I detections done with SOFIA (Serra et al. 2015a; Westmeier et al. 2021) were linked across a spatial and spectral radius of 2 with a minimum size requirement for a reliable source of 8 spatial pixels and 5 spectral channels. SOFIA's reliability filter was then applied to remove all detections with a reliability below 0.6, using a Gaussian kernel density estimator of size 0.3 times the covariance. All remaining sources were then parametrized, assuming a restoring beam size of 30 arcsec for all integrated flux measurements.

The resulting detections were inspected by eye to remove obvious artefacts that were unlikely to be genuine H I sources. Many of these artefacts are related to inadequate flagging of the upper-left and lower-left corner beams of the mosaic that have strayed into the region considered here. After manual removal of artefacts, 272 detections remain. This data set was released internally to the WALLABY team as hydra TR2.

We use the internal moment-0 maps (total line intensity across frequencies associated with the galaxy) produced (Fig. 1), the 3D mask cube, and the SOFIA source catalog. These formed the basis for a segmentation image, an image denoting which pixels belong to an object in the catalog. We replaced non-zero pixels in the mask cube, collapsed on the frequency axis, with the source identification in the SOFIA catalog to be used as the segmentation image input in STATMORPH (Rodriguez-Gomez et al. 2019, see Section 3). To compute the morphometrics, we use the moment-0 and the collapsed mask cutouts from SOFIA, not the full mosaic out of memory management considerations.

2.3 GALEX observations of hydra

Two fields were observed for the original All Sky Imaging Surveys with the *GALEX* telescope in both the FUV and NUV channels (1350-1750 and 1750-2800 Å, respectively) with 210s exposures (Fig. 2). Overlap with the WALLABY central FOV is good but not all the H I detections are covered by UV observations (30 out of 272). While 63 galaxies have non-zero morphometrics, only 30 galaxies overlap with GALEX data; the remainder is the result of morphometrics on the empty sky contribution. STATMORPH runs on a segmentation map; in this case, the H I one will measure morphometrics where no source flux is present. Some SWIFT observations exist but only cover a single galaxy in the H I field and thus were not used.

3 MORPHOMETRIC CATALOGS

An observational approach to characterizing galaxy appearances is 'non-parametric' or morphometric parameters. In essence, several authors and groups have tried to come up with parameters that can be applied to images that do not depend too much on resolution or a preconceived idea about the shape of the profile. These non-parametric or 'morphometric' parameters[1] can then be used as quantities to classify galaxies along the Hubble Tuning fork or to identify mergers in a population of galaxies.

The morphometric parameters considered here are concentration, asymmetry, and smoothness (CAS) from Conselice (2003), M_{20} and Gini from Lotz, Primack & Madau (2004), and the MID parameters from Peth et al. (2016) and Rodriguez-Gomez et al. (2019). We use the STATMORPH package described in Rodriguez-Gomez et al. (2019) to compute the morphometrics. We utilize a Gaussian smoothing kernel with a 1 pixel full width at half-maximum (6 arcsec) for both H I and UV implementations of STATMORPH. This choice is not critical for the work here as this input smoothing kernel is only used for the Sérsic profile fit in STATMORPH, the index of which we do not use here. Both H I and UV profiles are typically not well described with a Sérsic profile (cf. Leroy et al. 2008; Bigiel, Leroy & Walter

[1]A term first coined here Davenport (2015). The term 'morphometrics' originates from biology to describe animal appearance in quantitative form, e.g. 'length of fins' or how far the eyes are set apart.

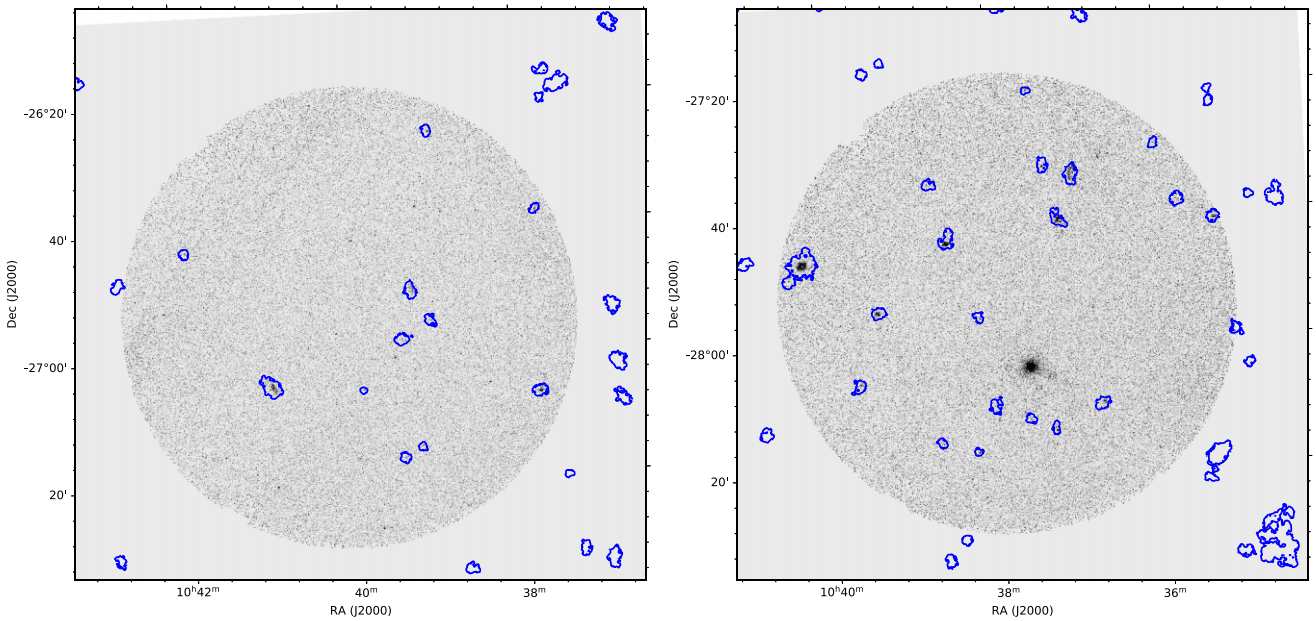

Figure 2. The FUV filter *GALEX* observations of the hydra cluster. H I detections are marked in blue (contour at 10 Jy/beam×Hz in the moment-0 map). There is an overlap of 30 H I detections in the *GALEX* fields with associated *GALEX* morphometrics. The bright FUV source in the second field is a foreground galactic star.

2011; Wang et al. 2014; Swaters et al. 2002, and Reynolds et al. in preparation for result of H I radial profiles).

In many cases, these morphometrics still require inputs other than the image. The relevant input parameters are the central position of the galaxy (x_c, y_c), and a definition of the area over which these parameters are computed, the segmentation of the image (i.e. which pixels belong to the object of interest). These two measurements, the centre of the object and which parts of the image belong to it, are often obtained from source extractor (Bertin & Arnouts 1996; Holwerda 2005).

Here, the segmentation map was generated from the the SOFIA 3D mask and the central positions were computed by STATMORPH. By using the H I map for the segmentation, the granular nature of the FUV/NUV imaging can be accounted for and the oversegmentation of the UV image can be avoided. The use of the H I contour effectively isolates distant galaxies from Galactic stellar sources. Foreground Galactic stars are less of a consideration (cf. Fig. 2).

3.1 Concentration-Asymmetry-Smoothness morphometrics

CAS refers to the now commonly used CAS space (Conselice 2003) for morphological analysis of distant galaxies. Concentration of the light, symmetry around the centre, and smoothness as an indication of substructure.

Concentration is defined by Bershady, Jangren & Conselice (2000) as:

$$C = 5\ \log(r_{80}/r_{20}) \tag{1}$$

with r_f as the radius containing percentage f of the light of the galaxy [see definitions of r_f in Bertin & Arnouts (1996), Holwerda (2005)]. In the optical, typical values for the concentration index are $C = 2$–3 for discs, $C > 3.5$ for massive ellipticals, while peculiars span the entire range (Conselice 2003).

The asymmetry is defined as the level of *point-* (or rotational-), symmetry around the centre of the galaxy (Abraham et al. 1994; Conselice 2003):

$$A = \frac{\Sigma_{i,j}|I(i,\,j) - I_{180}(i,\,j)|}{\Sigma_{i,j}|I(i,\,j)|} - A_{bgr}, \tag{2}$$

where $I(i, j)$ is the value of the pixel at the position $[i, j]$ in the image and $I_{180}(i, j)$ is the pixel at position $[i, j]$ in the galaxy's image; later, it was rotated 180° around the centre of the galaxy. In the STATMORPH implementation, the asymmetry is calculated in the inner 1.5 Petrosian[2] radii (tyical size of the stellar disc), the background asymmetry is subtracted, and A is minimized by moving the centre of rotation. This is a different implementation than used in Holwerda et al. (2012). Note that asymmetry maximum value is 2 (all pixels off-centre) and can be negative if the background asymmetry value is large. We note that we do not subtract a background when using the moment-0 H I maps as these are extracted from the field using the 3D source mask.

The fact that this smoothness has another input parameter in the form of the size of the smoothing kernel makes it highly 'tunable', meaning one gets out exactly what was optimized for. It is very difficult to reliably compare between catalogs or even implementations. For this reason, 'smoothness' is not considered further here.

3.2 Gini and M_{20}

Abraham, van den Bergh & Nair (2003) and Lotz et al. (2004) introduce the Gini parameter to quantify the distribution of flux over the pixels in an image. They use the following definition:

$$G = \frac{1}{\bar{I}n(n-1)}\Sigma_i(2i - n - 1)I_i, \tag{3}$$

[2]The Petrosian radius is one of several definitions to automatically assign a size and aperture to inherently fuzzy galaxies. For a comprehensive treatment on them, see Graham et al. (2005) and Graham & Driver (2005).

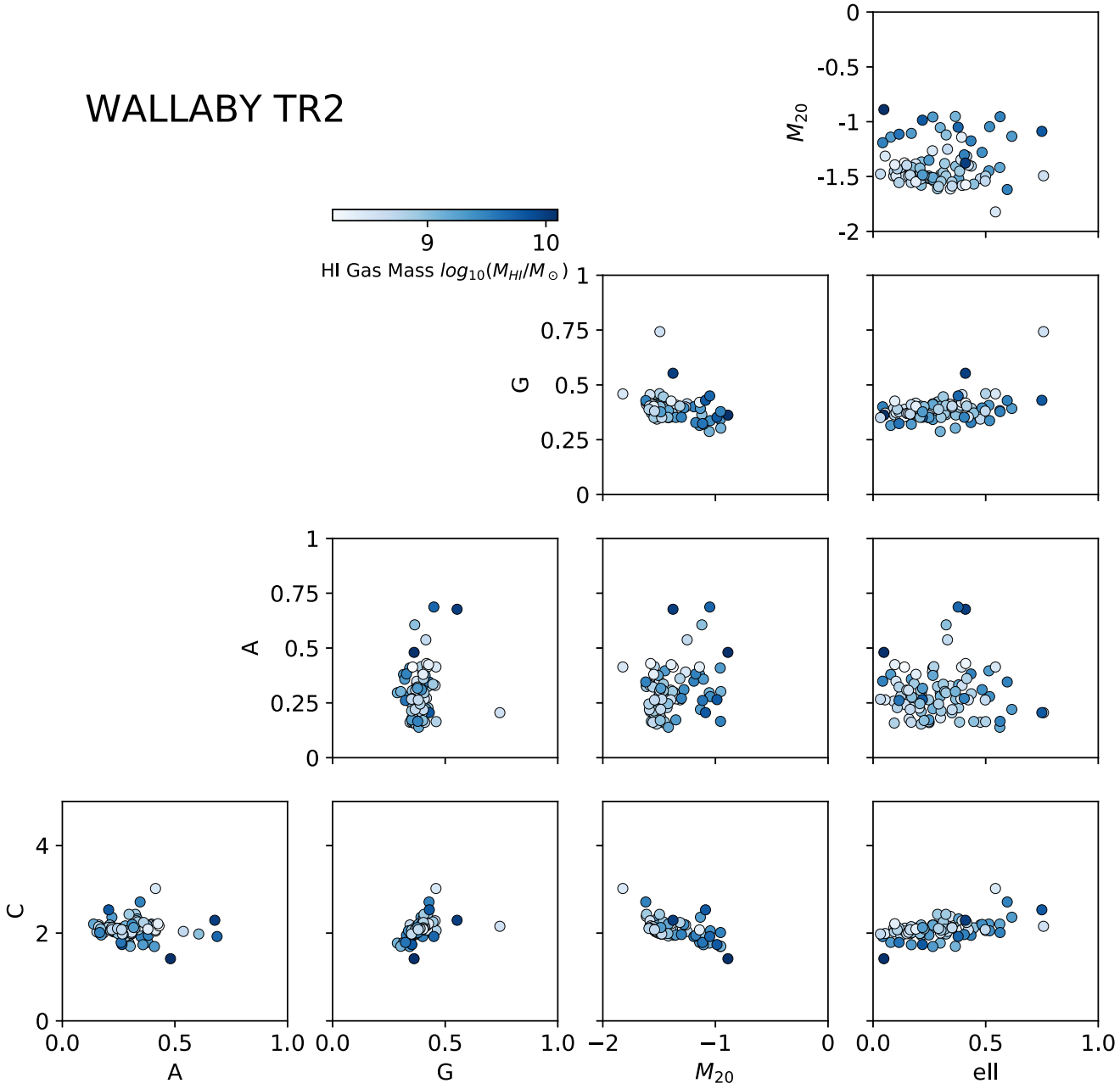

Figure 3. The H I morphometrics corner plot. Concentration, asymmetry, Gini, and M20 together with the ellipticity computed by STATMORPH with the H I mass from WALLABY.

I_i is the value of pixel i in an ordered list of the pixels, n is the number of pixels in the image, and $\bar{I}$ is the mean pixel value in the image. This is the computationally least expensive implementation where not the entire mosaic has to be loaded.

The Gini parameter is an indication of equality in a distribution (initially an economic indicator Gini 1912; Yitzhaki 1991), with G = 0 the perfect equality (all pixels have the same fraction of the flux) and G = 1 perfect inequality (all the intensity is in a single pixel). Its behaviour is therefore in between that of a structural measure and concentration. Gini appears quite sturdy as it does not require the centre of the object to be computed. It remains relatively unchanged, even when the object is lensed (Florian, Li & Gladders 2016), and it is popular for this reason. However, it depends strongly on the image's signal to noise (Lisker 2008). In essence, noise can add pixels with no fraction of the flux in them, artificially increasing the Gini value.

Lotz et al. (2004) also introduced a way to parametrize the extent of the light in a galaxy image. They define the spatial second-order moment as the product of the intensity with the square of the projected distance to the centre of the galaxy. This gives more weight to emission further out in the disc. It is sensitive to substructures such as spiral arms and star-forming regions but insensitive to whether these are distributed symmetrically or not. The second-order moment of a pixel i is defined as:

$$M_i = I_i \times [(x - x_c)^2 + (y - y_c)^2], \quad (4)$$

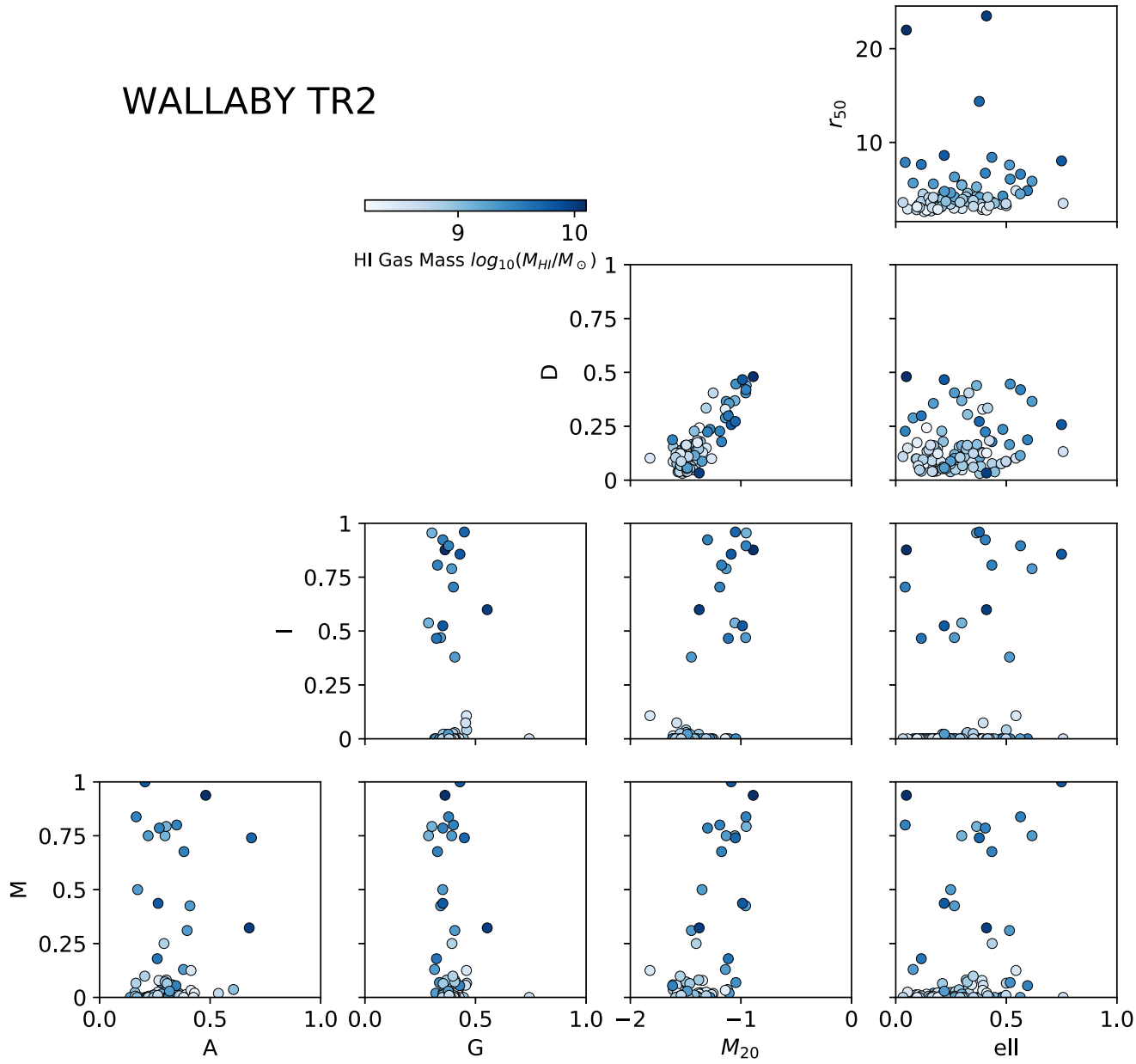

Figure 4. The MID morphometrics compared against the concentration-asymmetry-Gini-M_{20} of the H I morphometrics computed by STATMORPH with the H I mass from WALLABY.

where $[x, y]$ is the position of a pixel with intensity value I_i in the image and $[x_c, y_c]$ is the central pixel position of the galaxy in the image.

The total second-order moment of the image is given by:

$$M_{tot} = \Sigma_i M_i = \Sigma I_i[(x_i - x_c)^2 + (y_i - y_c)^2]. \quad (5)$$

Lotz et al. (2004) use the relative contribution of the brightest 20 per cent of the pixels to the second-order moment as a measure of disturbance of a galaxy after sorting the list of pixels by intensity (I_i):

$$M_{20} = log\left(\frac{\Sigma_i M_i}{M_{tot}}\right), \text{ for } \Sigma_i I_i < 0.2 I_{tot}. \quad (6)$$

The M_{20} parameter is sensitive to bright regions in the outskirts of discs and higher values can be expected in galaxy images (in the optical and UV) with star-forming outer regions as well as those images of strongly interacting discs.

3.3 Multimode-intensity-deviation morphometrics

The multimode-intensity-deviation (MID) morphometrics (Freeman et al. 2013; Peth et al. 2016) were introduced as an alternative to the Gini-M20 and CAS morphometrics to be more sensitive to recent mergers. However, these new morphometrics have not been tested as extensively as the Gini-M20 and CAS statistics, especially using hydrodynamic simulations (Lotz et al. 2008, 2010, 2011; Bignone et al. 2017); see also the discussion in the implementation in STATMORPH (Rodriguez-Gomez et al. 2019). In the case of H I data, none of the morphometrics have been extensively tested and are to be viewed as purely phenomenological.

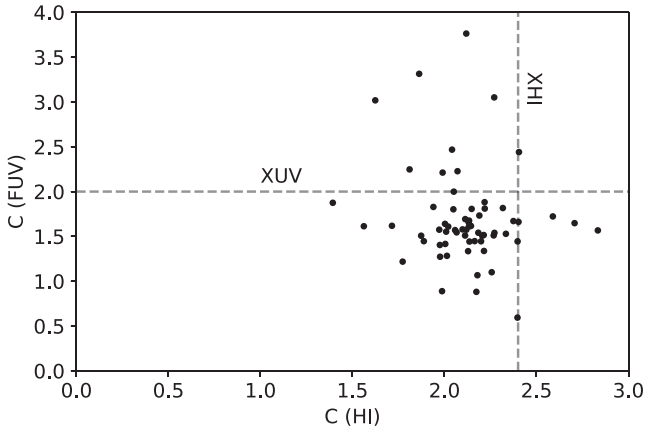

Figure 5. The concentration values for H I and FUV for the overlap in samples. Extended H I and UV discs potentially stand out by their high concentration value. The dashed lines are the criteria for extended sources from Holwerda et al. (2012).

Table 1. The galaxies with high concentration values in FUV (Fig. 5) and NUV with their asymmetry and M_{20} values. These are potential XUV discs in the hydra cluster. Asteriks indicates a candidate XUV discs based on the asymmetry and M_{20} values.

FUV cat id	C_{FUV}	A_{FUV}	$M_{20,\,FUV}$	C_{HI}	
J100720-262426	2.23	−3.27	−0.65	2.07	*
J101035-254920	3.02	−0.13	−1.31	1.62	
J101359-253824	2.44	−0.15	−0.87	2.40	*
J101434-274133	3.31	0.11	−1.40	1.86	
J101945-272719	3.05	0.26	−1.04	2.27	*
J102207-282201	2.47	−0.61	−1.04	2.04	*
J102413-284853	2.21	−0.21	−0.84	1.99	
J102600-280334	3.76	0.18	−0.73	2.12	*
J102605-280710	2.25	−1.92	−0.79	1.81	
NUV cat id	C_{NUV}	A_{NUV}	$M_{20,\,NUV}$	C_{HI}	
J100720-262426	2.21	−2.91	−0.79	2.07	
J101035-254920	2.83	0.03	−1.25	1.62	
J101359-253824	3.11	−0.04	−1.32	2.27	
J101434-274133	2.06	−0.05	−0.86	1.99	
J101945-272719	2.25	−1.28	−0.65	1.81	

Table 2. The galaxies with high-concentration values in H I (Fig. 5) but with no FUV or NUV counterpart. These are extended H I discs that may hold XUV discs in the hydra cluster.

cat id	C_{HI}	A	M_{20}
J100539-282633	2.47	0.40	−1.29
J100634-295615	2.52	0.36	−1.52
J102341-291347	2.45	0.39	−1.42
J102416-284343	2.41	0.46	−1.56
J103015-270743	2.55	0.39	−1.63
J103420-264728	3.02	0.41	−1.82
J103543-255954	2.49	0.63	−1.28
J103603-245430	2.43	0.32	−1.61
J103818-285023	2.71	0.35	−1.62
J103853-274100	2.80	0.63	−1.48
J103902-291255	2.43	0.30	−1.50
J103915-301757	2.53	0.21	−1.09
J104339-285157	2.76	0.24	−1.59
J104442-290119	2.89	0.39	−1.61
J104447-270553	2.42	0.43	−1.48

We explore them here because the UV morphology tends to be much more 'clumpy' than the optical one, and by using the H I outer contour, one can still consider such galaxies as a single object. The MID morphometrics were developed to identify mergers by distinct cores, not segregated by the segmentation, and may prove useful.

4 RESULTS

In this section, we discuss the two morphometric catalogs computed using the WALLABY H I data and the WALLABY and *GALEX* data combined.

4.1 H I morphometrics

Fig. 3 shows the distribution of the most commonly used morphometrics for the H I moment-0 map. There is a good range of values, despite the much lower dynamical range typically present in H I maps. The concentration values for H I are clustered around a value of 2. There is a full range of asymmetry values. Asymmetry is calculated with the inclusion of a background component by STATMORPH, but none is included here since the values in the moment-0 map not belonging to an object are set to zero. There are also reasonably high values for the Gini and M_{20} parameters, indicating a fair amount of substructure resolved by the WALLABY observations. Concentration and M_{20} are anticorrelated to some degree as can be expected because M_{20} upweighs pixels far from the centre. The range of ellipticity values indicates a wide distribution of viewing angles on the H I discs of these galaxies. These ellipticity values are based on second-order moments and not ellipse fitting of the H I cube. The H I morphometrics show a wide range in value. The only parameters that show a narrow range are concentration and Gini, which both can be attributed to the lower dynamic range of the moment-0 maps.

4.2 MID H I morphometrics

The MID morphometrics for the H I moment-0 maps are compared to the more traditional C-A-G-M_{20} in Fig. 4. Morphometrics were never meant to be an orthogonal parameter space, but these MID morphometrics may probe slightly different phenomena. Deviation and M_{20} are clearly correlated and multimode and intensity may be weakly correlated with M_{20} as well. Both multimode and intensity values are pre-dominantly close to 0, but there are notable outliers. These MID morphometrics, which are sensitive to substructure within an object, may prove to be useful for H I and UV science in addition to the other, original morphometrics developed for optical morphology.

4.3 Truncated and extended H I discs

Holwerda et al. (2011e) noted that H I computed concentration may be linked to H I stripping and truncation. Fig. 5 shows that relatively few galaxies in the overlap sample exhibit the low values of H I concentration ($C < 1.5$) associated with truncated H I discs. In the optical, the typical exponential disc value is $C = 2 - 3$, a spheroidal galaxy much higher.

We view these low-concentration H I discs as possibly truncated, similar to those observed by Chung et al. (2009) for the Virgo cluster at slightly higher spatial resolution (15 arcsec) with the VLA. Holwerda et al. (2011e) found in the VIVA data that low-concentration H I discs are more likely truncated.

Conversely, high values of concentration could be an indication of an extended H I or FUV disc. Fig. 5 shows high values for mutually exclusive subsamples (listed in Tables 1 and 2).

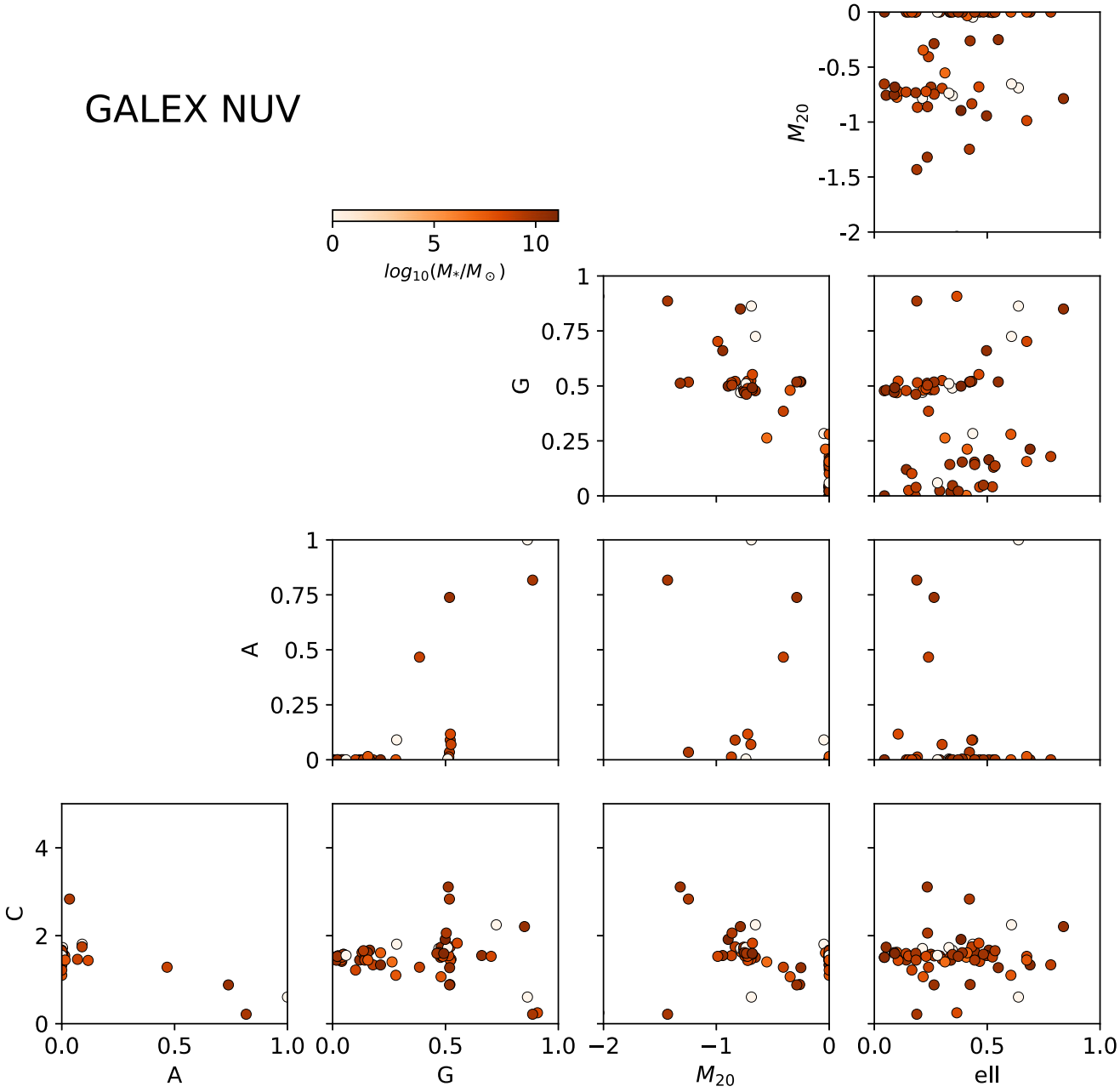

Figure 6. The distribution of NUV and FUV morphometric parameters for the objects with UV observations. There is NUV/FUV information on 30 objects (63 with catalog entries). Those with, e.g. A = 0, are the result of morphometrics on fixed pixel values of the area outside the FOV; they encode the H I shape. The colour bar is the stellar mass of these galaxies.

4.4 FUV morphometrics

Fig. 6 shows the corner plot for both FUV and NUV galaxies. Some of the objects included have unphysical values (e.g. A = 0) and are likely included despite no flux in the H I contour. In general, the NUV/FUV catalog is much smaller than the H I catalog (30 objects in the *GALEX* fields with 63 with non-zero *GALEX* morphometric values and 272 H I morphometric values), calculated for all the objects in GALEX footprint.

4.5 XUV disc candidates

Holwerda et al. (2012) noted that the H I outer contour is a good way to compute the UV morphology as it clearly delineates which UV clumps of emission belong to a disc galaxy and which do not. Fig. 7 shows the FUV M_{20} and asymmetry values with concentration colour-coded. If we use the $M_{20} - A$ criterion from Holwerda et al. (2012), very few objects in the hydra cluster fall under the XUV classification. However, the implementation of asymmetry differs from Holwerda et al. (2012). This emphasizes our point that for each survey, wavelength, and implementation, new criteria will need to be calibrated to identify objects of interest. Low values of asymmetry and M_{20} with high-concentration values will be the candidates for XUV discs. Holwerda et al. (2012) noted that the fraction identified and specific criteria used to identify XUV discs depends on both H I and UV depth and H I resolution (e.g. WHISPS versus THINGS resolution). Based on this initial identification, 5/32 galaxies (∼15 per cent, see Table 1) in the hydra cluster have an

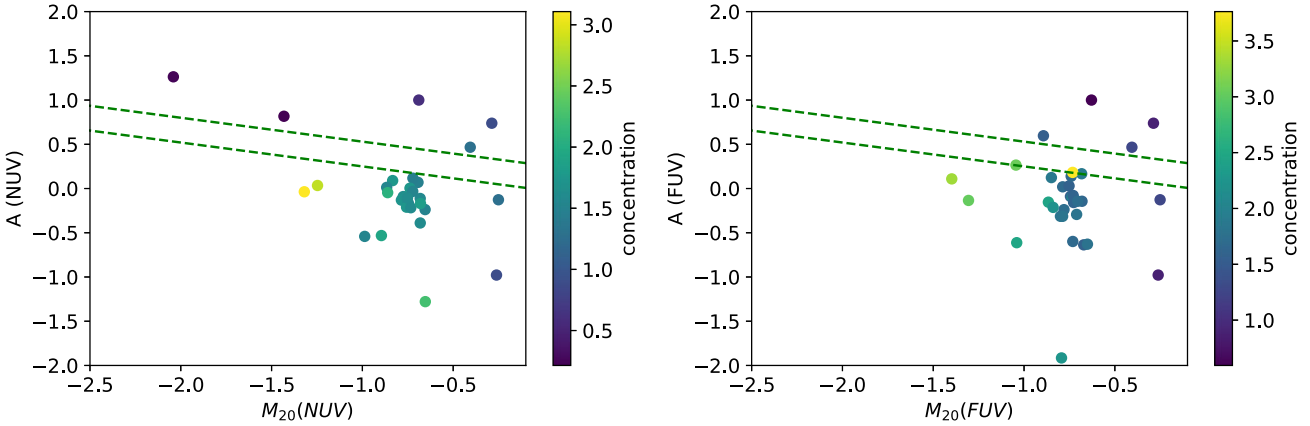

Figure 7. The asymmetry and M_{20} parameters from STATMORPH in the *GALEX* FUV and NUV channels with concentration colour-coded. The criterion identified by Holwerda et al. (2012) as potentially useful to identify XUV discs is marked with green dashed lines. In between these lines were the known XUV discs identified in their WHISPS/*GALEX* catalogs. Galaxies with high values of concentration, low values of asymmetry, and M_{20} are good candidates for XUV discs.

XUV disc, a substantial reduction (factor 5–6) compared to the field (Lemonias et al. 2011; Moffett et al. 2012).

Fig. 8 shows a few examples of FUV images of high FUV concentration with the WALLABY H I contour. It highlights how extended FUV sources can be found through computed apertures, but outer disc flux contributions will be missed without the H I contour definition. Even with the most shallow *GALEX* observations typically available (AIP 200 s) and greater distances than the resolved galaxies of THINGS and WHISP (Holwerda et al. 2012), one can identify extended UV discs through their morphometrics.

5 RAM-PRESSURE STRIPPING

Wang et al. (2021) present estimates of the RPS that H I galaxies in the hydra cluster are undergoing based on the same data. They use a holistic approach to classify galaxies as undergoing RPS using H I appearance, kinematics, and stellar-mass surface density. They flag galaxies undergoing RPS and candidate galaxies for undergoing RPS (RSP-r1). Figs 9 and 10 show the H I morphometric feature space with the RPS flag and candidate RPS flag (RPS-r1) indicated.

Both flags would be of interest for ML as one could use morphology to identify RPS without inspection or one could flag candidate RPS galaxies. In the H I morphometrics (Figs 9 and 10), the two populations are well-mixed, spanning the full ranges of values. It may well be that in the full feature space or a subset thereof, the two may well be separable. With no immediate clear separation in this parameter space, ML techniques developed to identify separation with a single hyperplane or a limited set of choices potentially could.

6 MACHINE LEARNING CLASSIFICATION OF RPS FROM H I MORPHOMETRICS

With a substantial feature space in the H I morphology and no immediate intuition on where RPS galaxies should lie within this space, we attempted to use the H I morphometric features to classify the RPS flags of Wang et al. (2021) using different ML classifier from SKLEARN (Pedregosa et al. 2011). The goal is to identify which H I morphometric parameters are best in pre-selecting RPS, what cuts in that space could lead to RPS candidates being identified in the remaining WALLABY survey, and how well ML can identify RPS in the H I feature space.

Because the non-RPS galaxies outnumber the RPS galaxies in the hydra catalogs, we balance the data using SMOTE in the IMBLEARN package, which supplements the SKLEARN one for ML. The sample is normalized (whitened) using SKLEARN's standard scaler. The sample is then split 80–20 per cent randomly for training and testing respectively (400/100 instances after SMOTE). This is a smaller sample than typical in ML applications. Our aim, however, is to evaluate the future applicability of the H I morphometrics feature space to identify RPS.

We apply a decision tree, k-nearest neighbour, a support-vector machine, and a random forest classifier to estimate how well one can distinguish RPS galaxies in the H I morphometric space. We calculate the accuracy (fraction of correct classifications), the precision (the fraction of true positives over true negatives), the recall (the fraction of true positives of total positives), and the F1 = (precision × recall) / (precision + recall). Before SMOTE to rebalance the data, the F1 scores were poor for all ML algorithms that follow.

6.1 Decision tree

A decision tree classifier is a series of criteria in feature space that ultimately split the training sample according to the labels provided. We split our hydra sample into 80 per cent training and 20 per cent test after SMOTE rebalancing. We trained on classifying either the RPS flag or the candidate RPS flag (RPS-r1) from Wang et al. (2021).

6.2 H I morphometrics decision tree

We tried two decision trees, one for the RPS flag and one for the candidate RPS flag (RPS-r1). Both went to over a dozen forks indepth. Every permutation of the H I morphometric feature space yielded a result (accuracy, precision, recall, and F1) with the test sample. These are summarized in Table 3, showing the accuracy (combined precision for positive and negative), precision (the fraction of selected positives correctly identified), recall (the fraction of positives correctly identified), and F1 (= precision × recall/precision + recall) metrics for each decision tree. Precision and recall are low for all trees, with Gini-R50 performing best for the RPS flag (f_{RPS}) and the C-A-G-M20 space for the candidate RPS flag ($f_{r1,\,RPS}$).

At present best, the H I morphometric feature space can identify about 80 per cent of the galaxies undergoing RPS (as identified by Wang et al. 2021). Similar to what we found in Holwerda et al. (2011e), there are multiple processes influencing the H I appearance and perhaps this feature space cannot do much better. However, the sample is still small compared to typical ML applications.

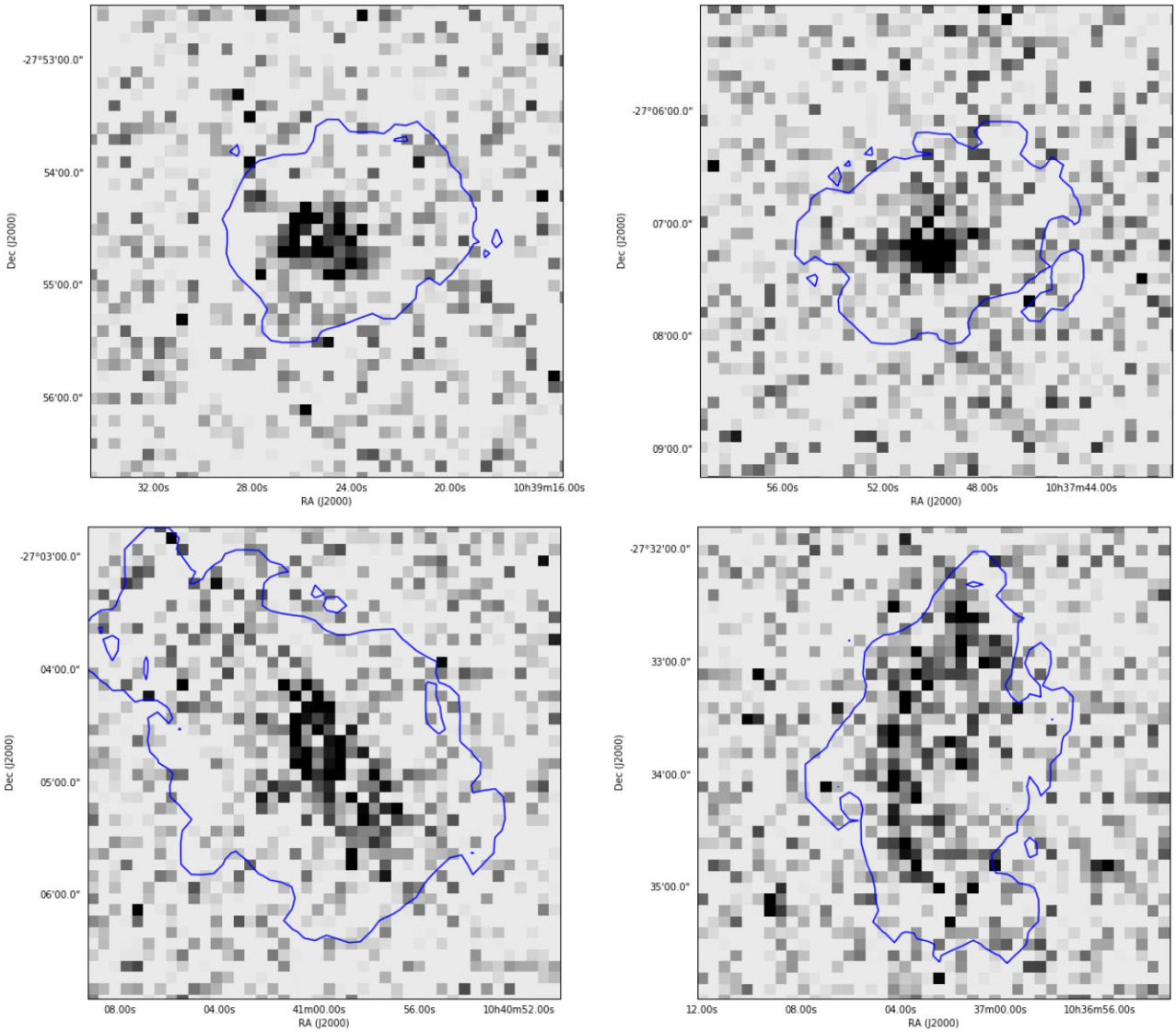

Figure 8. Examples of *GALEX* FUV cutouts with the H I contour overlaid. These are reliable XUV detections with high UV values of concentration. The top examples could have been detected using an optical isophote but lower examples show the benefit of an H I contour (10 Jy/beam×Hz). J103924-275442 (top-left), J103749-270715 (top-right), J104059-270456 (bottom-left), and J103702-273359 (bottom-right).

6.3 K-nearest neighbour (KNN) on H I morphometrics

K-nearest neighbour classifies using the N-nearest neighbours in the feature space. Table 4 shows the metrics for the RPS flag in different H I morphometrics with N = 3. Performance is similar or poorer than the decision trees; the precision is typically worse, the recall better, resulting in comparable F1 metrics. KNN classifiers works best in coherent, homogeneous, and isometric areas within the feature space. If the labels are sharply split in the feature space, this approach has less applicability.

6.4 Support vector machine on H I morphometrics

Support vector machine (SVM) is an ML algorithm optimized to disentangle labelled populations within a feature space. The SVM algorithm is to find a hyperplane in an N-dimensional space, where N is the number of features, which distinctly classifies the data points according to their labels (in this case RPS or not). We use the SKLEARN implementation of SVM to try to classify using the H I morphometrics.

The main hyperparameters regulating SVMs are the regularization parameter C_{reg} and the choice and tuning of a convolution kernel. We opt for 'sigmoid' kernel, the default, and a 'polynomial' one, and plot the metrics as a function of the regularization parameter in Fig. 11. Most combinations of feature space perform optimally around $C \sim 5$. The metrics for $C_{reg} = 5$ and the 'sigmoid' kernel for each different feature set are listed in Table 5 and 6. While the accuracy initially looks reasonably promising, both precision and recall leave much to be desired (neither realistically top 75 per cent). We note that the H I morphometrics catalog is still small for ML applications with 272 total entries and 148 with RPS classifications, and there is room for future improvements with larger samples.

Changing to a different kernel (from sigmoid to polynomial) does not improve performance.

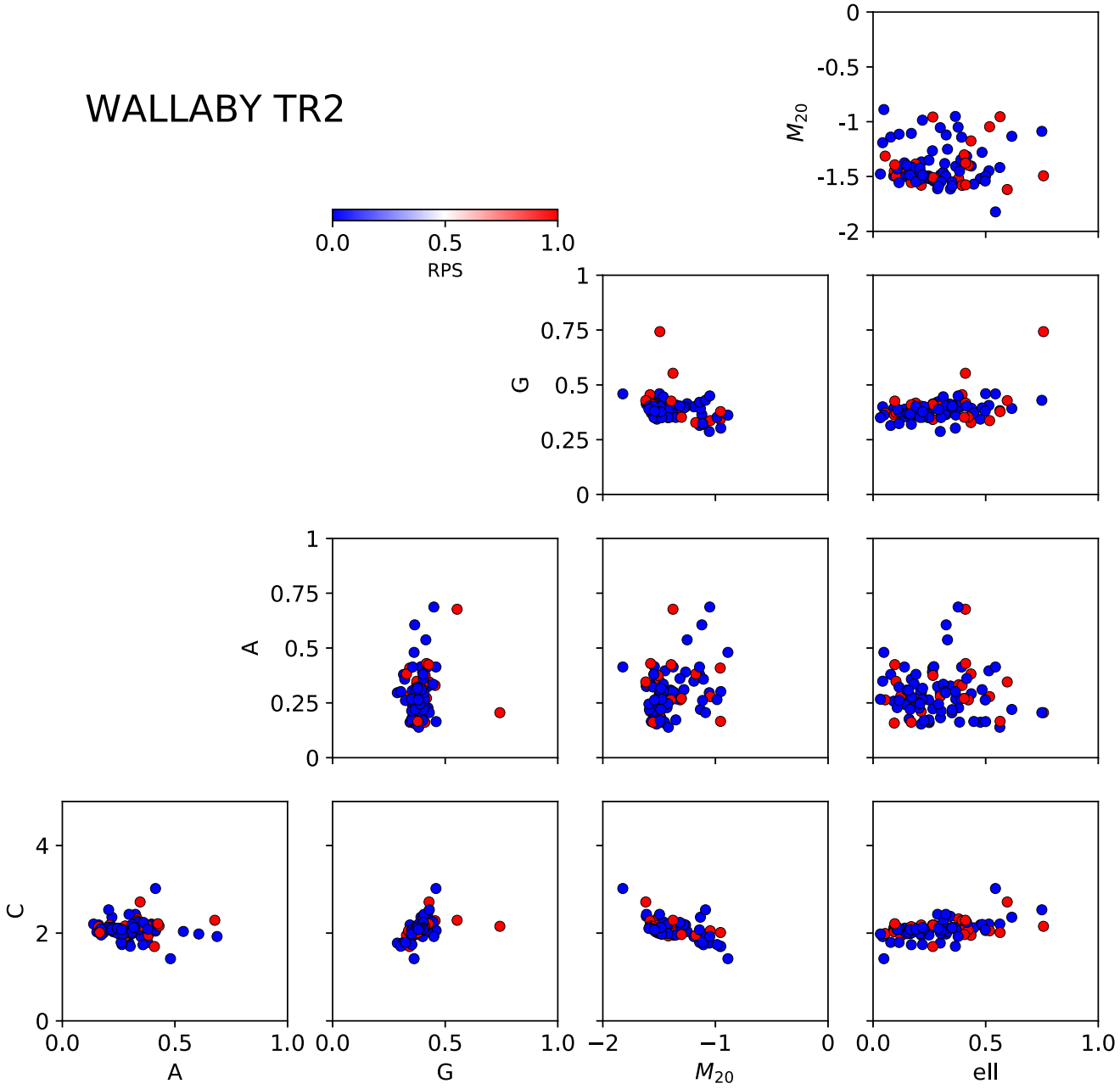

Figure 9. The C-A-G-M20-ellipticity H I morphometric feature space with the RPS flag from Wang et al. (2021) marked with the colour: red galaxies are undergoing RPS.

6.5 Random forest

A random forests is an ensemble ML method for classification that works by constructing a multiple decision trees at training time into an ensemble (trees combined into a forest). For classification, the output of the random forest is the class selected by most trees. It has the benefit of more robustness and less sensitivity to outliers in the training set. For our catalog classification, this is the final option before one resorts to classifications with the images as inputs with, e.g. convolutional neural networks, etc.

Table 7 shows the performance of the random forest for different choices of the parameter space. It performs quite well with rebalancing the training data. Similar results on classification based on these morphometrics for simulated *JWST* images came to a similar conclusion that morphometrics and a random forest are well paired (Rose in preparation).

7 CONCLUDING REMARKS

The initial quality of the hydra cluster WALLABY field is already enough to produce reliable morphology maps from the moment-0 (intensity) maps. We combined the H I information with *GALEX* imaging for 30 out of the 272 galaxies in the field. In this way, the H I information allows one to define the complete disc of galaxies, useful to identify which UV sources should be considered part of the galaxy and which are background sources (cf. the discussion of outermost H II regions in Hunter et al. 2018).

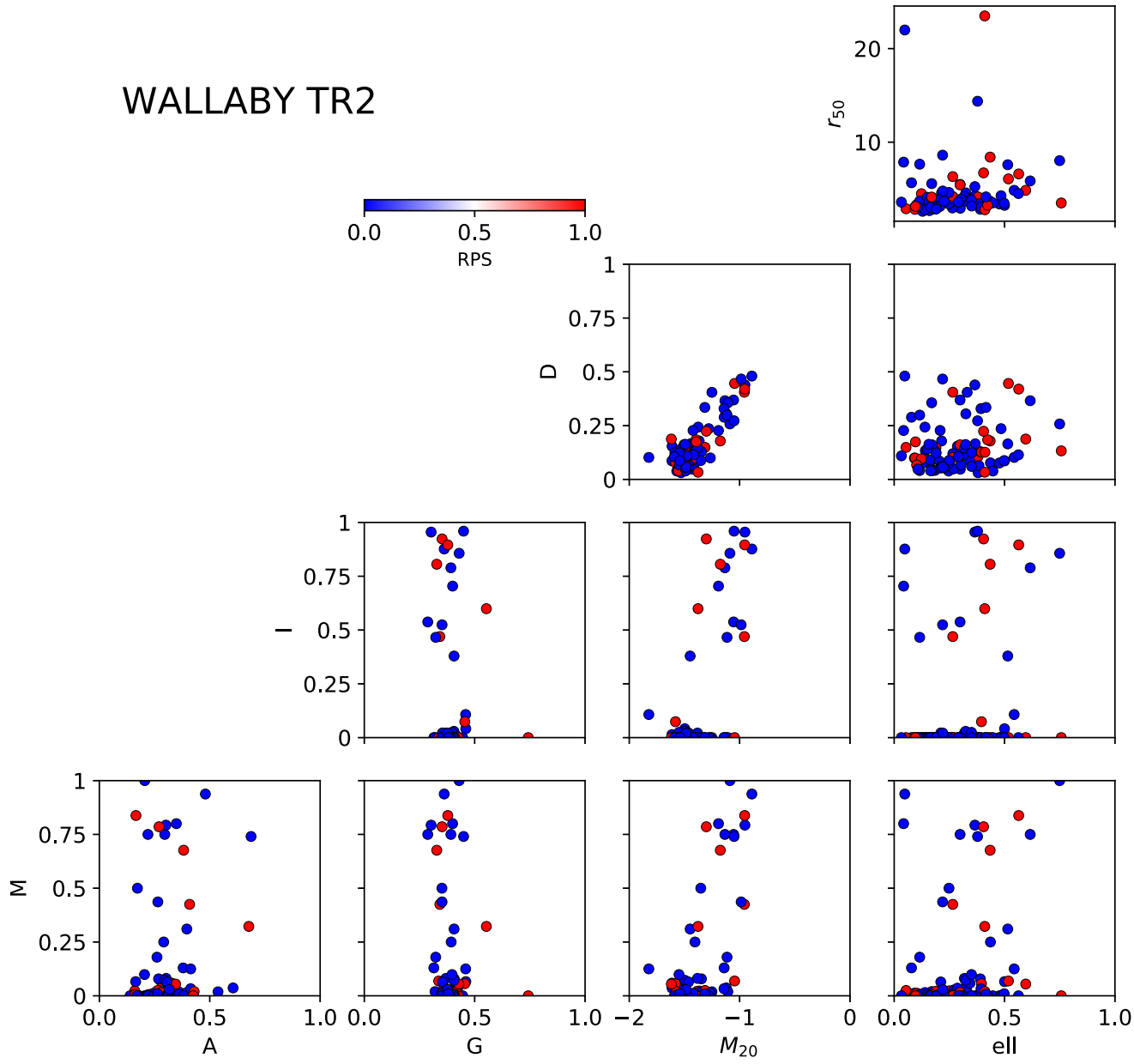

Figure 10. The M-I-D-ell H I morphometric feature space with the RPS flag from Wang et al. (2021) marked with the colour: red galaxies are undergoing RPS.

Table 3. The accuracy, precision, recall, and F1 metrics of the decision tree based on different feature choices to identify the unresolved and resolved RPS flags from Wang et al. (2021).

	Accuracy	Precision	Recall	F1
f_{RPS}				
HI C-A-G-M20-M-I-D-R50	0.80	0.71	0.89	0.39
HI C-A-G-M20	0.80	0.84	0.86	0.43
HI MID-R50	0.80	0.73	0.82	0.39
$f_{r1,\,RPS}$				
HI C-A-G-M20-M-I-D-R50	0.83	0.85	0.82	0.42
HI C-A-G-M20	0.78	0.80	0.80	0.40
HI MID-R50	0.80	0.80	0.82	0.41

Table 4. The accuracy, precision, recall, and F1 metrics of the kNN based on different feature choices to identify the unresolved and resolved RPS flags from Wang et al. (2021).

	Accuracy	Precision	Recall	F1
f_{RPS}				
HI C-A-G-M20-M-I-D-R50	0.76	0.65	1.00	0.39
HI C-A-G-M20	0.81	0.72	0.93	0.41
HI M-I-D-R50	0.74	0.64	0.93	0.38
$f_{r1,\,RPS}$				
HI C-A-G-M20-M-I-D-R50	0.80	0.75	0.92	0.41
HI C-A-G-M20	0.69	0.67	0.84	0.37
HI M-I-D-R50	0.74	0.74	0.80	0.38

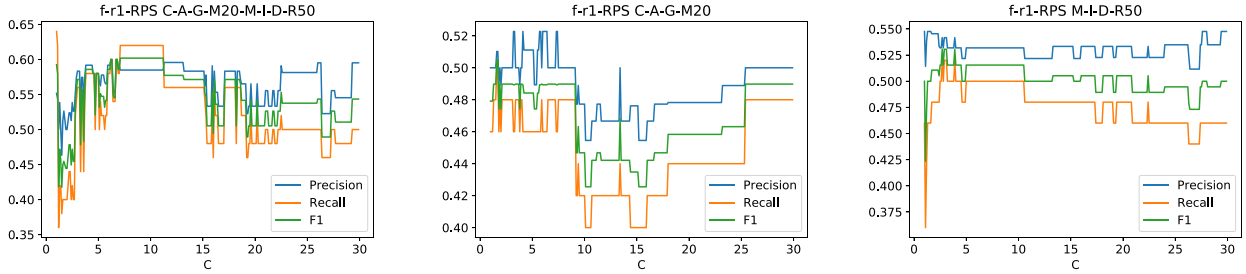

Figure 11. The metrics (precision, recall, and F1) as a function of the regularization parameter C_{reg} of the SVM for three instances of the feature space: CAGM20MIDR50, CAGM20, and MIDR50 for the r1-RPS flag from Wang et al. (2021). SVM performs poorly in separating RPS from non-RPS galaxies with every configuration of the feature space and regularization parameter C_{reg}.

Table 5. The SVM performance for different subsets of the feature space with fixed $C_{reg} = 5$. $F1 = 2 \times (\text{Recall} \times \text{Precision})/(\text{Recall} + \text{Precision})$ is the weighted average of precision and recall.

Features	Accuracy	Precision	Recall	F1
f_{RPS}				
C-A-G-M20-M-I-D-R50	0.74	0.66	0.86	0.37
C-A-G-M20	0.74	0.67	0.80	0.36
M-I-D-R50	0.64	0.56	0.89	0.34
$f_{r1,\,RPS}$				
C-A-G-M20-M-I-D-R50	0.61	0.63	0.66	0.32
C-A-G-M20	0.60	0.63	0.64	0.32
M-I-D-R50	0.49	0.62	0.16	0.13

Table 6. The SVM performance for different subsets of the feature space with fixed $C_{reg} = 5$ and a polynomial kernel convolution.

features	Accuracy	Precision	Recall	F1
f_{RPS}				
C-A-G-M20-M-I-D-R50	0.52	0.48	1.00	0.32
C-A-G-M20	0.51	0.47	1.00	0.32
M-I-D-R50	0.51	0.47	1.00	0.32
$f_{r1,\,RPS}$				
C-A-G-M20-M-I-D-R50	0.52	0.73	0.16	0.13
C-A-G-M20	0.56	0.55	0.94	0.35
M-I-D-R50	0.52	0.73	0.16	0.13

Table 7. The random forest performance for different subsets of the feature space.

features	Accuracy	Precision	Recall	F1
f_{RPS}				
C-A-G-M20-M-I-D-R50	0.84	0.74	0.98	0.42
C-A-G-M20	0.86	0.79	0.93	0.43
M-I-D-R50	0.71	0.62	0.91	0.37
$f_{r1,\,RPS}$				
C-A-G-M20-M-I-D-R50	0.78	0.78	0.84	0.40
C-A-G-M20	0.74	0.72	0.84	0.39
M-I-D-R50	0.77	0.78	0.80	0.40

The fraction of XUV discs in the Universe is a potential constraint on how many disc galaxies are still accreting gas to their outskirts and how many are not. The outermost disc remains an excellent edge-case for star formation in low-density ISM (Watson et al. 2016), a potential way to rejuvenate spheroidal galaxies (Moffett et al. 2012), and for tracing the chemical enrichment of disc galaxies (López-Sánchez et al. 2015).

Structural searches for XUV galaxy discs by Thilker et al. (2007) and Lemonias et al. (2011) find that some 20–30 per cent of spirals have an XUV disc and 40 per cent of S0s (Moffett et al. 2012), making this type of disc common but not typical for spiral and S0 galaxies. This is based mostly on local Universe data and on visual inspection (see also Thilker 2016) or a comparison with Spitzer radial profiles in deep imaging (Bouquin et al. 2015, 2018; Bouquin & de Paz 2016). However, with WALLABY and GALEX information combined, FUV morphometrics within the H I contour poses a viable way to identify these XUV discs (5/32, 15 per cent). The fraction of XUV discs is lower than in the field, typically ∼40 per cent. The pre-requisites are ASKAP H I and *GALEX* FUV imaging, where even the shallowest *GALEX* exposures are sufficient thanks to the accurate delineation using the outer H I contour using ASKAP.

We computed the morphometrics over the moment-0 maps for all 272 galaxies in the hydra TR2 catalog to act as the feature space to explore. A cluster population of galaxies at comparable distances with similar signal-to-noise limits on the observations is an ideal sample.

RPS is considered a principal avenue for galaxy transformation, in addition to tidal interactions, especially in dense environments. Identifying galaxies that are potentially undergoing RPS is therefore a motivator for H I (morphological) studies. We compare our morphometric feature space to the RPS labels from Wang et al. (2021) and find that ML classifiers – decision trees, SVMs, K-nearest neighbour, random forest – do not fully separate RPS galaxies in H I morphometric space yet. Decision trees are impractically deep and the SVM struggle with precision but this problem is slightly better with kNN and Random Forest (RF). On the whole, the performance is middling (e.g. ∼0.6 accuracy, precision, and recall for SVM) to fairly decent (∼0.8 for the RF and kNN). On the whole, it points that reasonably good performance (80 per cent precision and recall) is possible for populations and acceptable performance for individual galaxies, i.e. a ML algorithm, can give a probability it is undergoing ram pressure stripping) with a larger training set.

The feature space of H I morphometrics used is either the full (C-A-G-M20-M-I-D-R50), the first (C-A-G-M20), or second half (M-I-D-R50) of that space. No clear benefit of one grouping over the other in ML performance can be identified With the H I morphometric space and rather simple ML tools, one can identify populations of galaxies that are undergoing RPS reasonably well (precision and recall of ∼80 per cent). This may be useful to construct samples for further inspection but the performance is not yet good enough to reliably infer fractions of galaxies undergoing RPS throughout a survey without further checks. One of our original goals was to

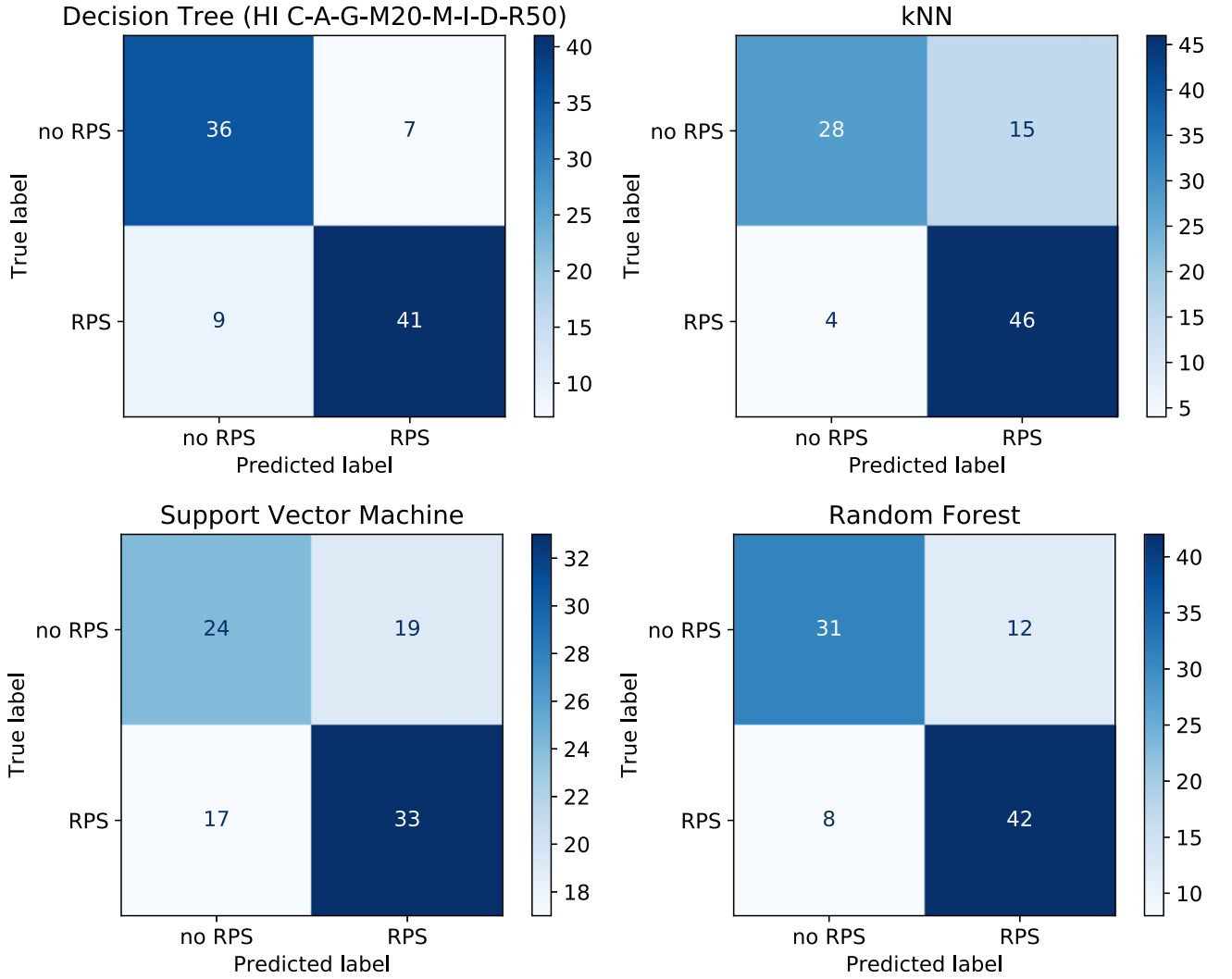

Figure 12. The classification matrices for the full H I feature space (C-A-G-M20-M-I-D-R50) and the r1-RPS flag from Wang et al. (2021) for the decistion tree, kNN, SVM, and RF.

ascertain whether this H I morphometric parameter space is good enough to aid in the identification of RPS galaxies. This appears to be feasible. Both larger test samples and possible direct use of the H I maps as input may improve results in the future.

(i) The morphometrics can be derived, even with the marginally resolved sources typical for WALLABY (Fig. 3).

(ii) They are a reasonably parameter space to identify galaxies that may be undergoing ram pressure (Fig. 3.

(iii) Using an H I contour for *GALEX* nearby galaxy data is a good segmentation choice (Fig. 8).

(iv) If the whole morphometric space is needed or a subset is viable is not yet clear (Table 3 – 7).

(v) A random forest is the best algorithm to classify based on the morphometric space. This has been found on *JWST* morphology papers as well independently. This saves substantial time/effort compared to convolutional neural networks, etc. (Fig. 12 and Table 7).

For the full WALLABY survey (Koribalski et al. 2020), one could apply these to all the solidly detected and partially resolved (e.g. 3–4 beams across) objects to create a parameter space for ML to identify populations such as galaxies undergoing RPS or gravitational interactions.

ACKNOWLEDGEMENTS

The Australian SKA Pathfinder is part of the Australia Telescope National Facility which is managed by CSIRO. Operation of ASKAP is funded by the Australian Government with support from the National Collaborative Research Infrastructure Strategy. ASKAP uses the resources of the Pawsey Supercomputing Centre. Establishment of ASKAP, the Murchison Radio-astronomy Observatory, and the Pawsey Supercomputing Centre are initiatives of the Australian Government, with support from the Government of Western Australia and the Science and Industry Endowment Fund. We acknowledge the Wajarri Yamatji as the traditional owners of the Observatory site.

This research made use of ASTROPY, a community-developed core PYTHON package for ASTRONOMY (Astropy Collaboration 2013, 2018).

AB acknowledges support from the Centre National d'Etudes Spatiales (CNES), France.

SHOH acknowledges a support from the National Research Foundation of Korea (NRF) grant funded by the Korea government (Ministry of Science and ICT: MSIT; No. NRF-2020R1A2C1008706).

FB acknowledges funding from the European Research Council (ERC) under the European Union's Horizon 2020 research and innovation programme (grant agreement No.726384/Empire)

BWH is supported by an Enhanced Mini-Grant (EMG). The material is based upon work supported by NASA Kentucky under NASA award No: 80NSSC20M0047.

BWH would like to thank Robin Allen and the teachers at Engelhart elementary for their hard work on distance learning during the COVID-19 lockdown and the game Minecraft for allowing for enough additional time to write this manuscript.

DATA AVAILABILITY

Electronic versions of the H I and UV morphometric catalogs and the segmentation map are included as supplemental information for this manuscript.

The full 30 square degree spectral-line cubes can be accessed on the CSIRO ASKAP Science Data Archive[3] (Chapman 2015; Huynh et al. 2020) with the DOI: https://doi.org/10.25919/5f7bde37c20b5 for this data set.

REFERENCES

Abraham R. G., Valdes F., Yee H. K. C., van den Bergh S., 1994, ApJ, 432, 75
Abraham R. G., van den Bergh S., Nair P., 2003, ApJ, 588, 218
Alberts S. et al., 2011, ApJ, 731, 28
Astropy Collaboration, 2013, A&A, 558, A33
Astropy Collaboration, 2018, AJ, 156, 123
Begeman K. G., 1989, A&A, 223, 47
Bershady M. A., Jangren A., Conselice C. J., 2000, AJ, 119, 2645
Bertin E., Arnouts S., 1996, A&AS, 117, 393
Bigiel F., Leroy A., Seibert M., Walter F., Blitz L., Thilker D., Madore B., 2010, ApJ, 720, L31
Bigiel F., Leroy A., Walter F., 2011, in Alves J., Elmegreen B. G., Girart J. M., Trimble V., eds, Symposium S270: Computational Star Formation, Proceedings of the International Astronomical Union, vol. 6, p. 327–334
Bignone L. A., Tissera P. B., Sillero E., Pedrosa S. E., Pellizza L. J., Lambas D. G., 2017, MNRAS, 465, 1106
Boomsma R., Oosterloo T. A., Fraternali F., van der Hulst J. M., Sancisi R., 2008, A&A, 490, 555
Bosma A., 1978, PhD thesis, Kapteyn Institute, University of Groningen
Bouquin A. Y. K., de Paz A. G., 2016, Proc. Int. Astron. Union., 11, 257
Bouquin A. Y. K. et al., 2015, ApJ, 800, L19
Bouquin A. Y. K. et al., 2018, ApJS, 234, 18
Bournaud F., Jog C. J., Combes F., 2005, A&A, 437, 69
Bresolin F., Ryan-Weber E., Kennicutt R. C., Goddard Q., 2009, ApJ, 695, 580
Bruzzese S. M., Meurer G. R., Lagos C. D. P., Elson E. C., Werk J. K., Blakeslee J. P., Ford H., 2015, MNRAS, 447, 618
Chapman J. M., 2015, in IAU General Assembly. p. 2232458, Available at https://ui.adsabs.harvard.edu/abs/2015IAUGA..2232458C
Chung A., van Gorkom J. H., Kenney J. D. P., Crowl H., Vollmer B., 2009, AJ, 138, 1741
Condon J. J., Cotton W. D., Greisen E. W., Yin Q. F., Perley R. A., Taylor G. B., Broderick J. J., 1998, AJ, 115, 1693
Conselice C. J., 2003, ApJS, 147, 1
Davenport J. R. A., 2015, I really want to find an astronomical application for morphometrics, https://twitter.com/jradavenport/status/571064841344917504 (Last accessed 2023 March 3)
de Blok W. J. G., Walter F., Brinks E., Trachternach C., Oh S.-H., Kennicutt R. C., 2008, AJ, 136, 2648
de Paz A. G. et al., 2008, in Funes J. G., Corsini E. M., eds, ASP Conf. Ser. Vol. 396, Astronomical Society of the Pacific Conference Series. Astron. Soc. Pac., San Francisco, p. 197
Dong H., Calzetti D., Regan M., Thilker D., Bianchi L., Meurer G. R., Walter F., 2008, AJ, 136, 479
Elagali A. et al., 2019, MNRAS, 487, 2797
Elson E. C., de Blok W. J. G., Kraan-Korteweg R. C., 2011, MNRAS, 415, 323
Ferguson A. M. N., Wyse R. F. G., Gallagher J. S., Hunter D. A., 1998, ApJ, 506, L19
Florian M. K., Li N., Gladders M. D., 2016, ApJ, 832, 168
For B. Q. et al., 2019, MNRAS, 489, 5723
Freeman P. E., Izbicki R., Lee A. B., Newman J. A., Conselice C. J., Koekemoer A. M., Lotz J. M., Mozena M., 2013, MNRAS, 434, 282
Giese N., van der Hulst T., Serra P., Oosterloo T., 2016, MNRAS, 461, 1656
Gil de Paz A. et al., 2005, ApJ, 627, L29
Gil de Paz A. et al., 2007, ApJ, 661, 115
Gini C., 1912, https://link.springer.com/article/10.1007/s10888-011-9188-x
Graham A. W., Driver S. P., 2005, Publ. Astron. Soc. Aust., 22, 118
Graham A. W., Driver S. P., Petrosian V., Conselice C. J., Bershady M. A., Crawford S. M., Goto T., 2005, AJ, 130, 1535
Heald G., Allan J., Zschaechner L., Kamphuis P., Rand R., Józsa G., Gentile G., 2011a, in Carignan C., Combes F., Freeman K. C., eds, IAU Symposium Vol. 277, IAU Symposium. p. 59
Heald G. et al., 2011b, A&A, 526, A118
Heiner J. S., Vázquez-Semadeni E., Ballesteros-Paredes J., 2014, MNRAS, 452, 1353–1374
Hess K. M., Kotulla R., Chen H., Carignan C., Gallagher J. S., Jarrett T. H., Kraan-Korteweg R. C., 2022, A&A, 668, A184
Hibbard J. E., van Gorkom J. H., Rupen M. P., Schiminovich D., 2001, in Hibbard J. E., Rupen M., van Gorkom J. H., eds, ASP Conf. Ser. Vol. 240, Gas and Galaxy Evolution. Astron. Soc. Pac., San Francisco, p. 657
Holwerda B. W., 2005, preprint (astro-ph/0512139)
Holwerda B. W., Pirzkal N., de Blok W. J. G., Bouchard A., Blyth S.-L., van der Heyden K. J., Elson E. C., 2011a, MNRAS, 416, 2401
Holwerda B. W., Pirzkal N., de Blok W. J. G., Bouchard A., Blyth S.-L., van der Heyden K. J., Elson E. C., 2011b, MNRAS, 416, 2415
Holwerda B. W., Pirzkal N., Cox T. J., de Blok W. J. G., Weniger J., Bouchard A., Blyth S.-L., van der Heyden K. J., 2011c, MNRAS, 416, 2426
Holwerda B. W., Pirzkal N., de Blok W. J. G., Bouchard A., Blyth S.-L., van der Heyden K. J., 2011d, MNRAS, 416, 2437
Holwerda B. W., Pirzkal N., de Blok W. J. G., van Driel W., 2011e, MNRAS, 416, 2447
Holwerda B. W., Pirzkal N., Heiner J. S., 2012, MNRAS, 427, 3159
Hotan A. W. et al., 2014, Publ. Astron. Soc. Aust., 31, e041
Hotan A. W. et al., 2021, Publ. Astron. Soc. Aust., 38, e009
Hunter D. A. et al., 2018, AJ, 156, 21
Huynh M., Dempsey J., Whiting M. T., Ophel M., 2020, in Ballester P., Ibsen J., Solar M., Shortridge K., eds, ASP Conf. Ser. Vol. 522, Astronomical Data Analysis Software and Systems XXVII. Astron. Soc. Pac., San Francisco, p. 263
Jog C. J., Combes F., 2009, Phys. Rep., 471, 75
Johnston S., 2007, in From Planets to Dark Energy: the Modern Radio Universe. October 1-5 2007. The University of Manchester, UK, p. 6 Published online at SISSA, Proceedings of Science
Johnston S. et al., 2007, Publ. Astron. Soc. Aust., 24, 174
Johnston S. et al., 2008, Exp. Astron., 22, 151
Johnston S., Feain I. J., Gupta N., 2009, in Saikia D. J., Green D. A., Gupta Y., Venturi T., eds, The Low-Frequency Radio Universe, ASP Conf. Ser., Vol. 407, proceedings of the conference held 8-12 December 2008, at NCRA, TIFR, Pune, India. Astron. Soc. Pac., San Francisco, p. 446
Kleiner D. et al., 2019, MNRAS, 488, 5352
Koda J. et al., 2015, ApJ, 802, L24
Koribalski B. S., 2017, in Gil de Paz A., Knapen J. H., Lee J. C., eds, Formation and Evolution of Galaxy Outskirts, Proceedings of the IAU Symposiumno. 321. p. 232
Koribalski B. S., 2022, invited ASKAP review at the 3rd URSI AT-AP-RASC, Gran Canaria
Koribalski B. S., López-Sánchez Á. R., 2009, MNRAS, 400, 1749
Koribalski B. S. et al., 2020, Ap&SS, 365, 118
Lee-Waddell K. et al., 2019, MNRAS, 487, 5248

[3]https://data.csiro.au/domain/casdaObservation

Lelièvre M., Roy J.-R., 2000, AJ, 120, 1306
Lemonias J. J. et al., 2011, ApJ, 733, 74
Leroy A. K., Walter F., Brinks E., Bigiel F., de Blok W. J. G., Madore B., Thornley M. D., 2008, AJ, 136, 2782
Lisker T., 2008, ApJS, 179, 319
López-Sánchez Á. R., Westmeier T., Esteban C., Koribalski B. S., 2015, MNRAS, 450, 3381
López-Sánchez Á. R., Lagos C. D. P., Young T., Jerjen H., 2018, MNRAS, 480, 210
Lotz J. M., Primack J., Madau P., 2004, AJ, 128, 163
Lotz J. M., Jonsson P., Cox T. J., Primack J. R., 2008, MNRAS, 391, 1137
Lotz J. M., Jonsson P., Cox T. J., Primack J. R., 2010, MNRAS, 404, 590
Lotz J. M., Jonsson P., Cox T. J., Croton D., Primack J. R., Somerville R. S., Stewart K., 2011, ApJ, 742, 103
McConnell D. et al., 2016, Publ. Astron. Soc. Aust., 33, e042
Meurer G. R., 2017, in Gil de Paz A., Knapen J. H., Lee J. C., eds, Formation and Evolution of Galaxy Outskirts, Proceedings of the International Astronomical Union, IAU Symposium, Vol. 321. p. 172, Cambridge University Press, Cambridge
Meurer G. R., Carignan C., Beaulieu S. F., Freeman K. C., 1996, AJ, 111, 1551
Meurer G. R., Staveley-Smith L., Killeen N. E. B., 1998, MNRAS, 300, 705
Meurer G. R. et al., 2009, ApJ, 695, 765
Moffett A. J., Kannappan S. J., Baker A. J., Laine S., 2012, ApJ, 745, 34
Moore E. M., Gottesman S. T., 1998, MNRAS, 294, 353
Noordermeer E., van der Hulst J. M., Sancisi R., Swaters R. A., van Albada T. S., 2005, A&A, 442, 137
Pedregosa F. et al., 2011, J. Mach. Learn. Res., 12, 2825
Peth M. A. et al., 2016, MNRAS, 458, 963
Planck Collaboration, 2016, A&A, 596, A100
Reynolds T. N. et al., 2019, MNRAS, 482, 3591
Reynolds T. N., Westmeier T., Staveley-Smith L., Chauhan G., Lagos C. D. P., 2020, MNRAS, 493, 5089
Reynolds T. N. et al., 2021, MNRAS, 505, 1891
Rodriguez-Gomez V. et al., 2019, MNRAS, 483, 4140
Sancisi R., Fraternali F., Oosterloo T., van der Hulst T., 2008, A&AR, 15, 189
Serra P. et al., 2015a, MNRAS, 448, 1922
Serra P. et al., 2015b, MNRAS, 452, 2680
Stinson G. S., Dalcanton J. J., Quinn T., Gogarten S. M., Kaufmann T., Wadsley J., 2009, MNRAS, 395, 1455
Swaters R. A., van Albada T. S., van der Hulst J. M., Sancisi R., 2002, A&A, 390, 829
Thilker D. A., 2016, Proc. Int. Astron. Un., 11, 298
Thilker D. A. et al., 2005a, ApJ, 619, L67
Thilker D. A. et al., 2005b, ApJ, 619, L79
Thilker D. A. et al., 2007, ApJS, 173, 538
van Eymeren J., Jütte E., Jog C. J., Stein Y., Dettmar R. J., 2011a, A&A, 530, A29
van Eymeren J., Jütte E., Jog C. J., Stein Y., Dettmar R. J., 2011b, A&A, 530, A30
Walter F., Brinks E., de Blok W. J. G., Bigiel F., Kennicutt R. C., Thornley M. D., Leroy A., 2008, AJ, 136, 2563
Wang Y., Ferland G. J., Lykins M. L., Porter R. L., van Hoof P. A. M., Williams R. J. R., 2014, MNRAS, 440, 3100
Wang J. et al., 2021, ApJ, 915, 70
Watson L. C., Martini P., Lisenfeld U., Böker T., Schinnerer E., 2016, MNRAS, 455, 1807
Watts A. B., Meurer G. R., Lagos C. D. P., Bruzzese S. M., Kroupa P., Jerabkova T., 2018, MNRAS, 477, 5554
Werk J. K., Putman M. E., Meurer G. R., Thilker D. A., Allen R. J., Bland-Hawthorn J., Kravtsov A., Freeman K., 2010, ApJ, 715, 656
Westmeier T. et al., 2021, MNRAS, 506, 3962–3976
Yitzhaki S., 1991, Am. Stat. Assoc., 9, 235
Zaritsky D., Christlein D., 2007, AJ, 134, 135
Zaritsky D., Rix H.-W., 1997, ApJ, 477, 118
Zschaechner L. K., Rand R. J., Heald G. H., Gentile G., Kamphuis P., 2011, ApJ, 740, 35

SUPPORTING INFORMATION

Supplementary data are available at *MNRAS* online.

sofia_morphometrics.csv

Please note: Oxford University Press is not responsible for the content or functionality of any supporting materials supplied by the authors. Any queries (other than missing material) should be directed to the corresponding author for the article.

This paper has been typeset from a TEX/LATEX file prepared by the author.